2nd International Joint Conference on Water Distribution Systems Analysis & Computing and Control in the Water Industry
Valencia (Spain), 18-22 July 2022
doi: https://doi.org/10.4995/WDSA-CCWI2022.2022.14127

ADVANCING TOWARDS SEMI-AUTOMATIC LABELING OF GPR IMAGES TO IMPROVE VISUALIZATIONS OF PIPES AND LEAKS IN WATER DISTRIBUTION NETWORKS USING MULTI-AGENT SYSTEMS AND MACHINE LEARNING TECHNIQUES

Gemma Stanton[1] and David Ayala-Cabrera[2]

[1,2] CWRR-School of Civil Engineering, University College Dublin, Dublin (Ireland)

[1] *gemma.stanton@ucdconnect.ie*, [2] *david.ayala-cabrera@ucd.ie*

Abstract

Critical infrastructures such as water distribution networks (WDNs) require reliable and affordable information at a reasonable cost to address challenges that can negatively affect their operation. Inadequate knowledge about WDN assets and their state of health presents challenges for essential activities such as network modeling, operation, assessment, and maintenance. This work seeks to increase the availability of WDN asset data through improved interpretability of GPR images. The semi-automatic labeling approach presented here expands upon existing multi-agent image-cleaning methods and feature characterization techniques. The division of a pre-processed image, in the form of a matrix, into a grid of smaller blocks allowed the identification of relevant features using density of nonzero values in the blocks; this approach, conducted manually in this proof of concept, can provide a basis for training an intelligent system (e.g., a convolutional neural network) to extract the families of interest and eliminate noise. Thus, this research expands this methodology to advance towards automatic detection of pipes and leaks and easily visualize the data. In this paper, 3D visualizations of WDN assets have been created to demonstrate the usefulness of this semi-automatic process in delivering easily-interpretable GPR data for managers and operators of WDNs.

Keywords

Water distribution networks, GPR image interpretation, 3D pipe models, Non-destructive testing methods, Water leakage, Intelligent data analysis, Multi-agent systems, Semi-automatic labeling of GPR images.

1 INTRODUCTION

Critical infrastructure such as water distribution networks (WDNs) present many challenges in their construction, operation, and maintenance. Effective management of these infrastructures requires economical, accessible, and reliable information [1] for decision-making processes. Information on the health of WDNs supports general operation activities such as modeling, operation, assessment, and maintenance [2] as well as resilient response to climate change [3], increasing digitization [4], and other such advances. WDNs and other buried assets may be difficult to assess and even locate, since manual inspection requires intensive labor and often necessitates excavation and significant social and economic disruption and even safety risks to carry out [5]. Minimizing the negative impacts of disrupting the WDNs and related infrastructure (*e.g.*, roads) is imperative [6] and calls for the incorporation of non-destructive testing methods to gather compile data on WDN health. Thus, non-destructive testing methods have been incorporated into the surveys to address the need for non-invasive procedures that provide relevant information on buried assets, including WDNs, gas pipelines, and more [7]. Non-destructive testing methods such as ground penetrating radar (GPR) are easy to deploy, but they present several difficulties (*e.g.*, absence of consistent GPR data interpretation protocols,

excessive noise, and heterogeneity of environmental conditions and equipment settings [8]) in the data interpretation process.

GPR is a non-destructive testing method which is deployable in a variety of environmental conditions (*e.g.,* urban environments [9]) and does not require disruption in the operation of the critical infrastructure inspected; *e.g*., water supplies in WDN [1]. GPR is examined in this research as an alternative to destructive testing to obtain relevant information regarding buried assets of WDN due to its potential to detect components (*e.g.,* pipes) and their integrity with great detail (*e.g.,* pipe with water leak [10], clogged pipe [11], deteriorated pipe [12]). Among the main advantages of the GPR as a non-destructing method, its inspection ability for successfully inspect different pipe materials has been evidenced in several studies (see [11, 12, 13]). GPR signals are capable of detecting materials, both metallic and non-metallic [14] (*e.g.*, PVC, asbestos cement, polyethylene), which are commonly used in assets of WDNs. GPR has the sensitivity to detect leaks in the media surrounding pipes [8], and this non-destructive method also offers accurate depth estimation and has an advantage of high resolution of up to a centimeter [15]. In the field of leak detection, other non-destructive methods such as thermography and tracer gas are limited by temperature, leak depth, and disruption to WDNs [16]. Furthermore, GPR is an inexpensive and non-destructive method, and it is easy for unskilled personnel to operate. However, the raw images produced by current GPR method require personnel with expertise to interpret them, increasing the cost and time that this method demands for analysis, and causes human interpretation errors [17]. While current GPR analysis requires expert interpretation, innovative processing methods can facilitate overcome this barrier.

Reliable data about WDNs can help their managers make responsible asset management decisions on when and how to make repairs and maintenance. Additionally, leak detection through GPR image analysis has the potential to prevent (*i.e.* by favoring the detection of water leaks at early stages) the waste of water, energy, and infrastructure [18] in those leaks that can only be identified when damage to a road surface occurs (i.e. when leaked water is visible [19). A raw GPR image may be used to detect and characterize a variety of subsurface assets (e.g. pipes of drinking water [20], gas [21], among others), but it is not easily interpretable, particularly for unskilled personnel as mentioned above. Although the raw GPR images are difficult to interpret, they contain a wealth of data that can be processed to extract useful information [22]. The work presented in this paper will serve managers and operators of WDNs who need accurate information about their networks. Basic data such as size and layout of pipes as well as material, interior build-up, leakage, and illegal connections can be detected more easily with this image cleaning technology.

The generation of 3D models of buried assets is an important final step in GPR data analysis since a key motivation of this work is to enhance site safety and deliver interpretable information for any operator without expertise [23, 24]. The 3D models generated from the information obtained after processing the GPR images can be used to feed augmented reality visualizations that can facilitate the assets assessment process [25] in a dynamic manner. The literature has examples of 3D model generation ranging from simple raw data plotting [16] to contours created from a series of pre-processed cross sections [8, 26]. These contours created from pre-processed cross sections are a significant step towards interpretable GPR images; however, they rely on comparison of initial and final states of leaking pipes to extract the relevant features and construct a 3D image. In this work, this comparison is eliminated from the process using semi-automatic extraction of relevant features and reconstruction of cross-sectional profiles in 3D space. The results displayed here will demonstrate that it is possible to reconstruct 3D representations of buried pipes from a single set of GPR data collected at a the same time period.

2 METHODS

This section presents the treatment of GPR data proposed in this paper both for the semi-automatic labeling of the information and its previsualization in a 3D model. The generation of 3D models from GPR images can consist of 6 steps of which the current paper focuses particularly on the semi-automatic labeling, through a density boundary extraction, and its subsequent 3D model previsualization (see *Figure 1*). Each step of this process is described in the subsections below.

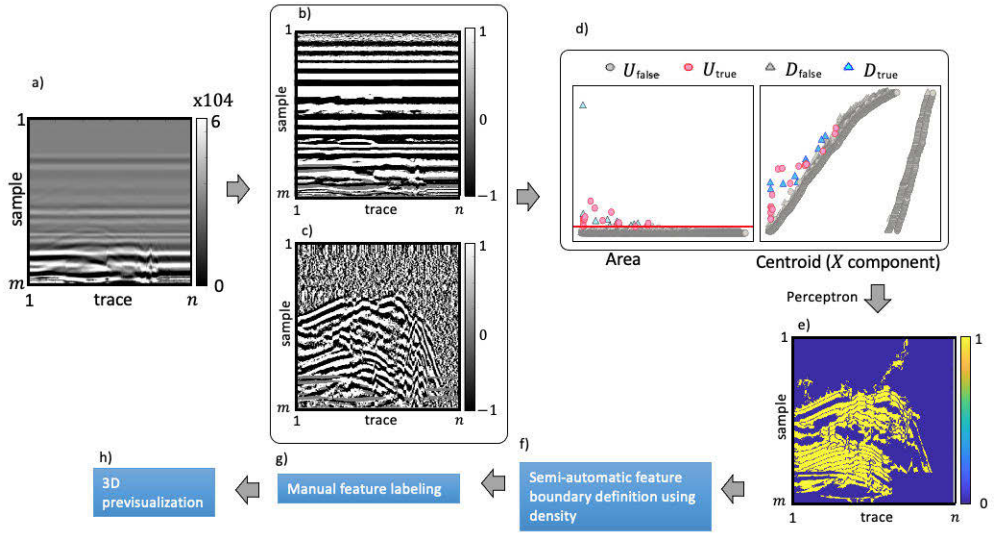

Figure 1. Proposed semi-automatic labeling of GPR images and 3D model previsualization. a) Raw GPR image, b) multi-agent pre-processing (vertical direction), c) multi-agent pre-processing (horizontal direction) d) semi-automatic feature extraction, e) semi-automatic feature extraction (visualization), f) semi-automatic labeling: density boundary, g) manual feature labeling, and f) 3D previsualization.

2.1 Raw GPR Images

GPR functions by propagating electromagnetic waves from a transmitter antenna below the ground at a specific velocity which is related to the medium through which it travels [7]. Parts of these waves return to a receiver antenna whenever an interface between two different media is reached; the wave is then partly propagated to deeper layers [17]. The reflected electromagnetic wave that is received by the receiver antenna has an amplitude proportional to the dielectric constant of the media through which it travels; a reflection at an interface between two materials correspond to a change in wave amplitude [22]. Thus, a raw GPR image, or radargram, contains a record of all the wave amplitudes recorded by a receiver in a matrix, A, of size m by n, where m represents the total two-way travel time of all the received signal of each trace ($i = 1, \dots, m$) and n corresponds to the total of traces captured ($j = 1, \dots, n$) with the survey (see Figure 1). A naked eye is unlikely to detect a hyperbola in a radargram, making these images difficult to interpret without processing.

2.2 Pre-Processing

[27] developed a multi-agent algorithm called “agent race” based on game theory to reduce the dimensionality of matrix A and prepare it for feature detection. This multi-agent algorithm pre-processes the radargram based on wave amplitudes intensity, as shown in Figure 2. The result of this algorithm is an $m1 \times n$ matrix (see Figure 2, Output 1), where the key features are registered

as movements of the agents in each *j* trace, and m1 represents the maximum total of movements obtained by the agent winner of the competition.

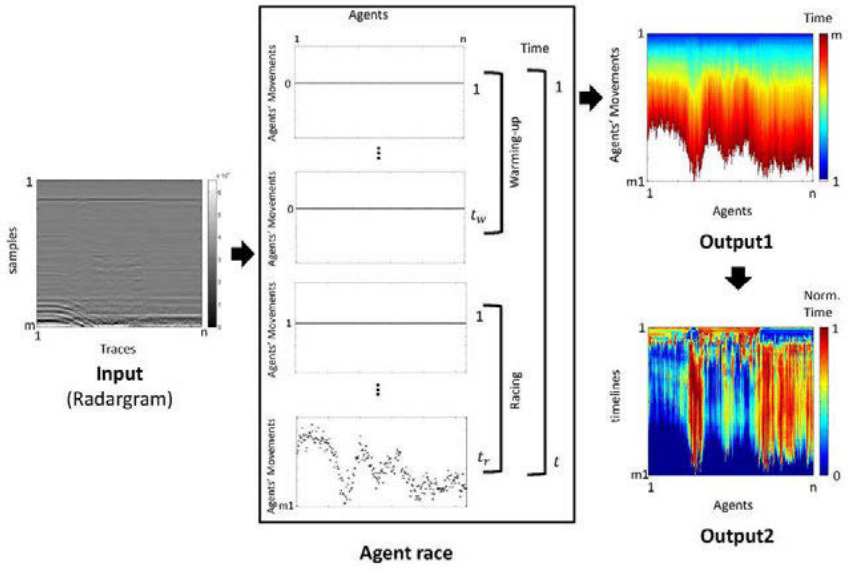

Figure 2. Agent race algorithm process. Adapted from [10].

The uses of the multi-agent pre-processing described above can generate groups (families), that contain features (in the form of functions) that specifically represent noise, horizontal lines, and objects (Figure 1, insets b and c). According to [28], agents run their moves on the rows of the *A* matrix (see the output in Figure 1c) and not on the columns (as it originally designed, see the output in Figure 1b) the removal of families that contain horizontal lines from these GPR images can be obtained. This removal was completed in [28] and [29] with the incorporation of noise removal through the use of perceptron neural network. In these studies, the geometric properties of the generated groups were used both to label (Area) and as a key feature for classification (*X* component of the centroid) of them (see Figure 1d).

Separating the noise and horizontal lines from the raw GPR images allows further analysis to detect features of interest in the objects group without the hindrance of noise and horizontal lines. This can be observed by comparing the raw GPR image (Figure 1a) with the resulting preprocessed image, *A*' matrix (Figure 1e). The $m \times n$ matrix *A*' (pre-processed image), consists of 0 and 1 values, where nonzero values indicate a feature of the target objects.

2.3 Semi-Automatic Labeling and Refinement

Labeling is an essential task in machine learning, in particular when the classification is conducted via supervised learning. This pre-preprocessing activity is conducted on various occasions manually as a preamble for the classification (via machine learning methods) of the embedded objects into the GPR images (*e.g.*, subsoil background [20], metallic and no- metallic pipes [31], among others). In order to reduce the dependency on personnel with high experience in interpreting GPR images and minimize the human errors that the manual labeling can generate, the analysis of densities is proposed as an alternative in this paper. In this sense, the GPR images cleaned by both the agents and the perceptron (see Section 2.2.), that had horizontal lines and noise removed, were used in this section as the starting point for the semi-automatic labeling proposal and to generate images that can be more easily interpreted.

Families of functions that represent embedded objects (*e.g.*, pipe objects) were preserved in *A*' matrix. These families contain additional information about the objects beyond the initial hyperbola identification that is commonly used to label the objects embedded into the GPR images [10, 32]. However, many of these families exist in the images and further analysis is necessary to

extract and classify those families of interest. In order to locate the features of interest, the proposed density analysis can be formulated as in equation (1) [19].

$$B_{ir,jr} = \sum_{iy_{ir}}^{iy_{ir+1}} \sum_{jx_{jr}}^{jx_{jr+1}} \left(\frac{a'_{(iy_{ir},iy_{ir+1}],(jx_{jr},jx_{jr+1}]}}{(iy_{ir+1} - iy_{ir} + 1)(jx_{jr+1} - jx_{jr} + 1)} \right) \quad (1)$$

In there, the pre-processed images in A' were further processed by dividing them into a grid of blocks ($a'_{iy,jx}$) with size $iy = \{1{:}\frac{m-1}{ly}{:}m\}$ (the step in y-axis) by $jx = \{1{:}\frac{n-1}{lx}{:}n\}$ (the step x-axis). Where ly and lx represents the dimension of the new matrix, B, generated for the blocks. Each block in B consists of $ir = \{1, \dots, ly\} \in \mathbb{N} = \{1,2,3 \dots\}$ and $jr = \{1, \dots, lx\} \in \mathbb{N} = \{1,2,3 \dots\}$. In essence, B represents the density calculation of nonzero values, from A', in each grid block. Figure *3* presents an example of a grid of 75×75 blocks which represents the subdivision of matrix A' (inset a) and the density of each block in a color scale (inset b).

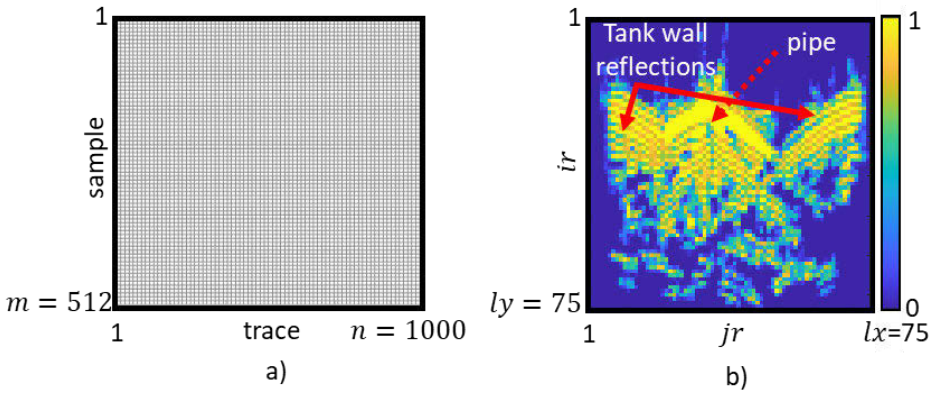

Figure 3. Generation of the density matrix B. a) Grid of 75×75 *blocks* ($ly = lx = 75$) *for A' matrix and, b) the respective densities; matrix B.*

The example presented in Figure *3* corresponds to a GPR image of a pipe buried in a wooden tank to emulate the phenomena of water leaks. More detailed information is presented in Section 3. Figure *3*b the hyperbola in the center of the image corresponds to the pipe itself, and is the most dense part of the figure. This detection of the hyperbola by the density method proposed herein, in addition to the highlighting of the tank reflections on the sides, shows the use of density as a useful tool for extracting features from GPR images.

Matrix B can be rescaled to the dimension of the original matrix A' (*i.e.*, from size of $ly \times lx$ to size of $m \times n$). Based on the observation of the densities generated by the object in the resulting matrix B (resized), it is proposed to iteratively determine a density threshold for each object. This thresholding generates groups that are captured by using the Matlab's `bwboundaries` function. In this work, we have selected the boundary of the group with the largest area as a representative element of the desired object to be extracted.

This extraction process can be used to label certain and particular objects of the GPR image in order to feed more robust classification processes. Likewise, these labels can be used to refine the pre-processing process presented above. This will allow the inclusion of new parameters to be considered, among other advantages. In addition, it is already possible to preview these images in 3D models as a preamble to automatic visualizations and it is in this sense that we will discuss about this process in Section 3.

3 CASE STUDY

In this section, we present both the application of the proposed GPR image labeling procedure and its results through 3D reconstructions. To do this, we have used as a case study the work presented in [10], where GPR images of a pipe leaking water were collected (at different stages of maturity of the phenomena) in a laboratory set up, depicted in Figure 4. In this configuration, a PVC pipe with diameter 100 mm and length of 0.95 m with one hole drilled to mimic a leak in the pipe and two points water input (WI) and water output (WO) was buried in dry soil in a wood tank (with size of 1.0 m × 1.0 m × 0.70 m). The tank was covered in a polypropylene plate with eleven paths parallel to the X-axis (transversal paths) and eleven paths parallel to the Y-axis (longitudinal paths), each path spaced 0.10 m from the next. A GPR (with a central frequency of 1.5 GHz) was run over each path as shown in Figure 4c, s5. Two samples of each of the 22 profiles were taken, one set without water in the setup and one set with water in the pipe and leakage around it. These two sets of samples are referred to as without water and with water, respectively.

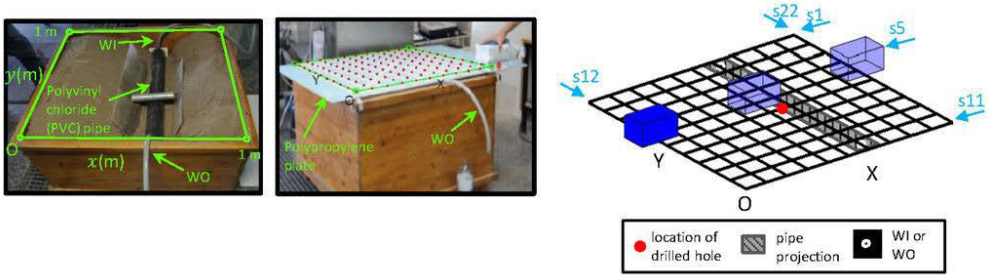

a) b) c)

Figure 4. Tank configuration (from [10]).

Density-boundary analysis. By using the density boundary procedure described in Section 2.3 and adjusting the number of blocks (both ly and lx) and density threshold, the pipe reflections were removed from transverse images to capture the boundary of the relevant feature (pipe, leak or tank reflection). Figure 5a shows a transversal profile, as an example, in which the boundary includes both the pipe and the tank reflections. Figure 5b shows how removing the tank reflections on the periphery of the central hyperbola allowed the pipe boundary to be captured.

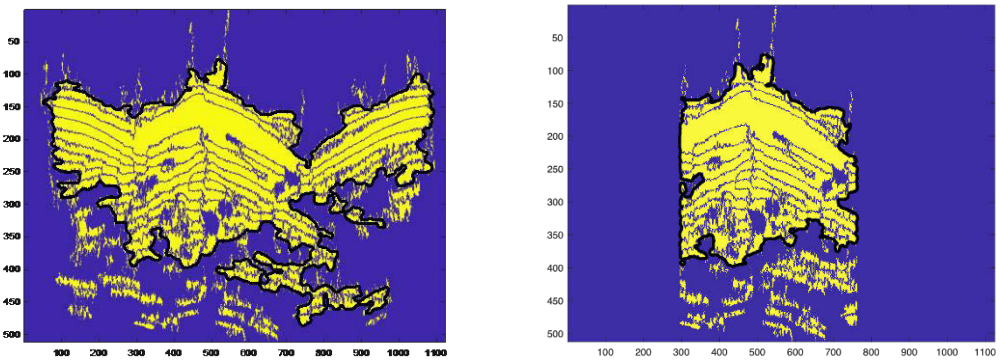

a) b)

Figure 5. Example of the labelling of the pipe in Profile 11 (s11) with the use of density-boundary process. a) before peripheral tank reflection removal and, b) after peripheral tank reflection removal.

The step and the density affect the resolution with which the boundaries of the features will be traced. The y blocks (ly) and x blocks (lx) the required density to locate the relevant features in each profile were adjusted manually in order to determine the optimal values for each parameter. The adjustments to these parameters ensured that the boundary of the relevant feature would be

as accurate as possible. For example, Figure 6 shows how increasing the x and y blocks from 40 (Figure 6a) to 100 (Figure 6b) increases the precision of the boundary.

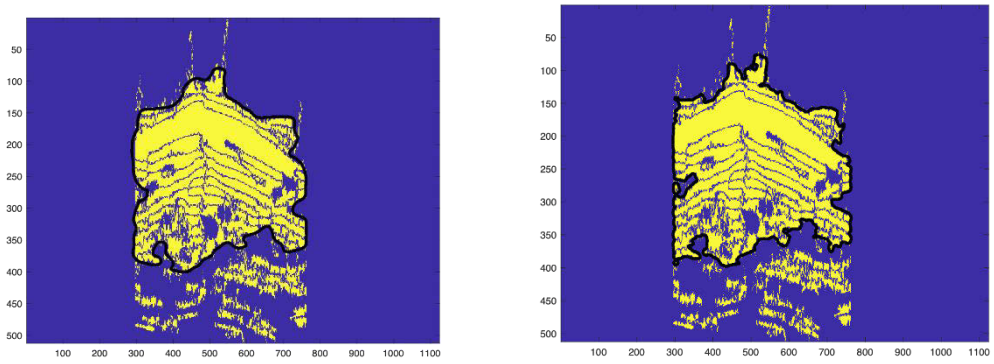

a) b)

Figure 6. Profile 11, a) $ly = lx = 40$ and, b) $ly = lx = 100$.

Some images contained spots of noise that would be included in the boundary if the required density of the feature was low (close to a value of 0); increasing the density would skip over this noise. In addition, a very high density (close to a value of 1) would skip over relevant parts of the desired boundary. Figure 7 illustrates the results for three density values.

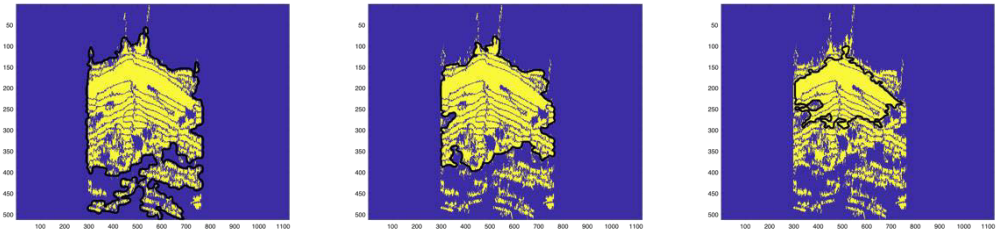

a) b) c)

Figure 7. Profile 11, a) density threshold=0.1 b) density threshold=0.4 and, c) density threshold=0.8.

For the profiles taken without water, the only boundaries identified were the tank reflection and the pipe.

Preliminary classification. The three main classes of objects in the profiles are tank reflection, pipe, and leak. It should be noted that in longitudinal profiles (s12-s22), pipes are represented as horizontal lines, and thus are removed in the pre-processing stage. As a result, no pipe classes exist in the longitudinal profiles. These classes were identified for each boundary in order to produce a clear 3D image. For the profiles taken with water into the system, boundaries obtained fell into five classes:

- Pipe,
- Leak,
- Pipe+leak (this due to difficulty in separating the two in one of the profiles),
- Tank reflection,
- Tank reflection+ leak (this due to difficulty in separating the two in one of the profiles).

The process of identifying boundaries based on determining an appropriate grid size and density threshold was conducted on transversal profiles (s1-s11). For the case of the system with water, the boundaries obtained for s1-s11 are displayed in Figure 8.

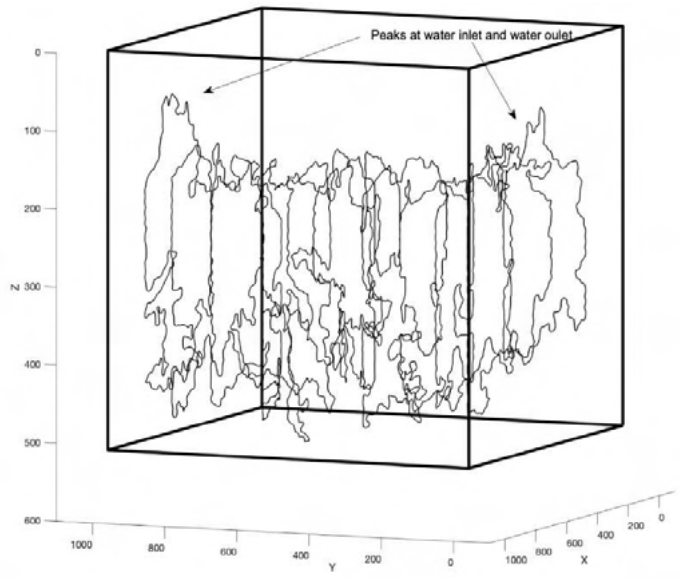

Figure 8. Boundary of pipe/pipe+leak for each transversal profile.

In Figure 8, the inlet and outlet for the system with water can be seen as peaks in the first and last profile. In [10], these peaks at the inlet (Figure 9a) and outlet (Figure 9k) are also observed in the images obtained through initial/final (without/with water into the system) image contrast. The capacity to identify the boundaries of the objects embedded into the GPR images without the requirement of a reference image to contrast, is one of the main virtues of the system proposed in this paper.

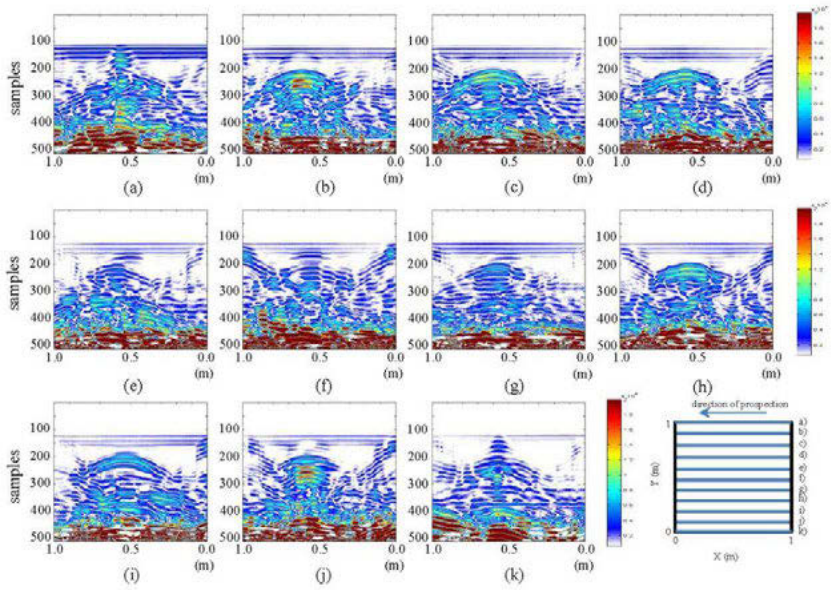

Figure 9. Images obtained using contrasts between initial and final states for transversal images (from [10]).

3D Image Construction. After the boundaries of these features were obtained, they were plotted in 3D space. The `interp2` function in Matlab was used to interpolate between 2D profiles. The known distance from the tank edge was inserted as *X* (for longitudinal) and *Y* (for transversal) coordinates. These distances are based on the GPR operator's selection of surface lines along which to take profile data. The interpolation between the boundaries of each profile without and with leakage in the transversal direction yielded the results in Figure 10(insets a and b; respectively).

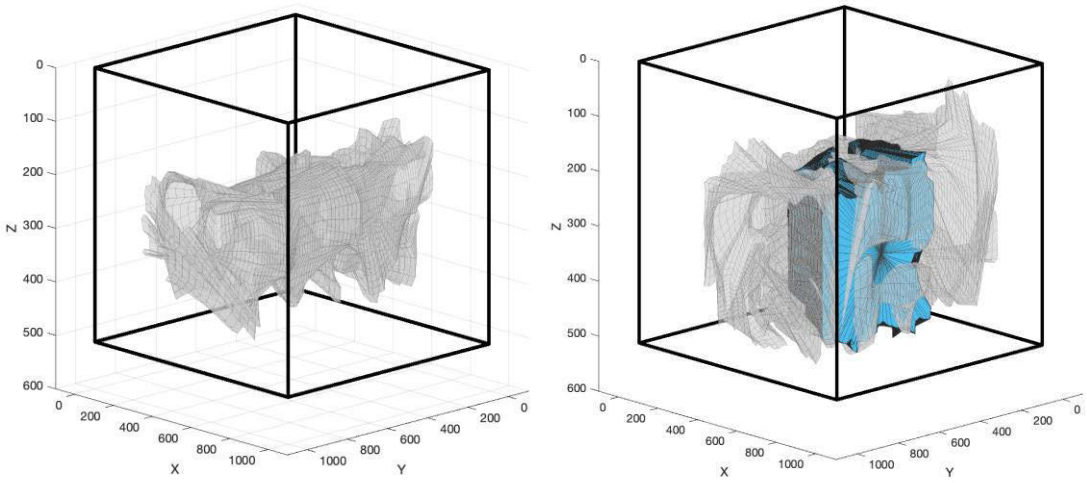

Figure 10. 3D reconstruction of pipe and leak for a) without water and b) with water into the system.

The pipe and leakage are clearly visible in the 3D image. The pipe/leakage representation in the transversal direction (gray) extends laterally past the leakage from the longitudinal direction (blue) in a few points as a result of the leakage from the longitudinal direction being difficult to capture in several profiles due to comprising disconnected shapes. For example, Figure 11 displays spots that represent the leak, that were not dense enough to be captured as one unit.

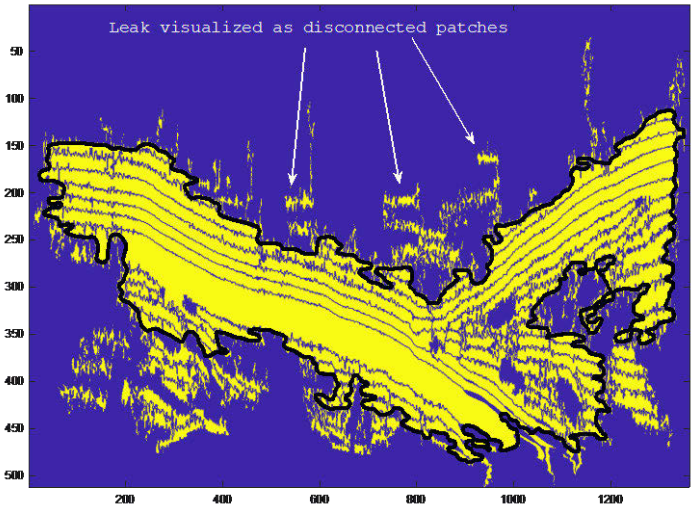

Figure 11. Profile 20, with tank reflection outlined by the boundary and leaks faintly represented.

Figure 12 presents the success in outlining the tank reflections in the longitudinal direction by means of the proposed semi-automatic labeling process. Outlining these reflections was useful to characterize their shape in the pre-processed GPR images, and may allow conversion to their real shape (a box) in the future.

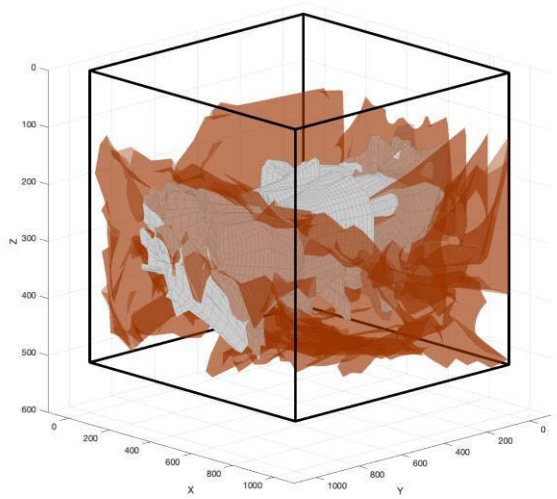

Figure 12. Representation of pipe and tank reflections for the system without water.

A few difficulties arose in the reconstruction of the 3D images from GPR data. For example, the sizes of the radargram matrix A for each profile had the same n dimension and varying m dimensions. This variation was due to the speed at which the GPR was run along the profile, taking a 120 traces/second, regardless of the total distance covered. This resulted in the first 3D reconstructions being askew. This problem was remedied by incorporating the estimated spatial coordinates for each trace in the analysis. However, the interpolation used in this reconstruction resulted in some inaccuracies due to the number of points in each cross section. For example, the interpolation between profiles 4 and 5 resulted in the constriction of the diameter of the profile as shown in Figure 13. This discrepancy in the interpolation may be resolved through the use of another interpolation function that will be tested in future work.

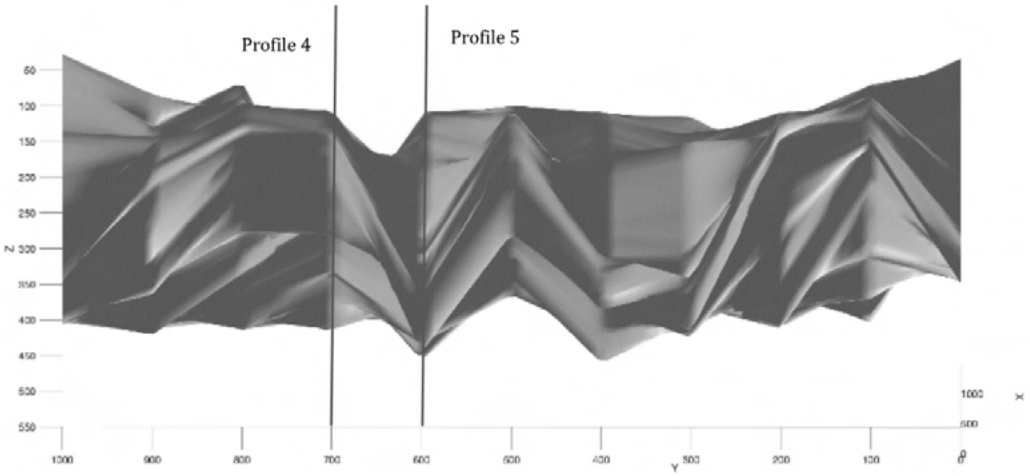

Figure 13. Transversal 3D image in Y-Z plane.

4 CONCLUSIONS

This approach to 3D image construction from GPR data began with a radargram matrix of the raw GPR data that was pre-processed using multi-agent techniques. The semi-automatic labeling of relevant features was conducted manually on the pre-processed images using the numerical approach of assessing the density of nonzero values in the pre-processed matrix. By extracting desired boundaries manually and plotting these, the need for initial/final state comparison was eliminated. Basic identification of classes was also possible due to the manual extraction and

classification of boundaries. This semi-automatic approach to labeling through density of grid blocks, as explained, offers a potential pathway to machine learning.

5 REFERENCES

[1] A. Aijazi, L. Malaterre, L. Trassoudaine, T. Chateau, and P. Checchin, "Automatic Detection and Modeling of Underground Pipes Using a Portable 3D LiDAR System," Sensors, vol. 19, no. 24, Dec. 2019, pp. 1-21.

[2] J. Liang, Q. Liu, H. Zhang, X. Li, Z. Qian, M. Lei, X. Li, Y. Peng, S. Li, and G. Zeng, "Interactive Effects of Climate Variability and Human Activities on Blue and Green Water Scarcity in Rapidly Developing Watershed," Journal of Cleaner Production, vol. 265, Aug. 2020, pp. 1-13.

[3] M. Karl, E. Culbertson, and J. Abrera, "Optimize Water Distribution Pipes and Water Loss with Digital Solutions," Journal AWWA, vol. 113, no. 7, Sept. 2021, pp. 69-73.

[4] P. Lau, B. W. Y. Cheung, W. W. Lai, and J. Sham, "Characterizing Pipe Leakage with a Combination of GPR Wave Velocity Algorithms," Tunnelling and Underground Space Technology, vol. 109, no. 1, Mar. 2021, pp. 1-12.

[5] T. Hao, C.D.F. Rogers, N. Metje, D.N. Chapman, J.M. Muggleton, J.Y. Foo, P. Wang, S.R. Pennock, P.R. Atkins, S.G. Swingler, J. Parker, S.B. Constello, M.P.N. Burrow, J.H. Anspach, R.J. Armitage, A.G. Cohn, K. Goddard, P.L. Lewin, G. Orlando, M. Redfern, A.C.D. Royal, and A.J. Saul, "Condition Assessment of the Buried Utility Service Infrastructure," Tunnelling and Underground Space Technology, vol. 28, Mar. 2012, pp. 331-344.

[6] S. Kerwin and B. Adey, "Optimal Intervention Planning: a Bottom-Up Approach to Renewing Aging Water Infrastructure," Journal of Water Resources Planning and Management, vol. 146 no. 7, Jul. 2020, pp. 1-16.

[7] M. Gupta, M. A. Khan, R. Butola, and R. M. Singari, "Advances in Applications of Non-Destructive Testing (NDT): a Review," Advances in Materials and Processing Technologies, Apr. 2021, pp. 1-22.

[8] D. Ayala-Cabrera, J. Izquierdo, S.J. Ocaña-Levario, and R. Pérez-García, "3D Model Construction of Water Supply System Pipes Based on GPR Images," in Proc. 7th International Congress on Environmental Modelling and Software, San Diego, C.A., USA: iEMSs, 2014.

[9] P. Song, Z. Pu, B. Ren, X. Tang, and J. Wang, "Application of Transient Electromagnetic Method in Municipal Buried Gas Pipelines Detection," in Proc. ASME 2020 Pressure Vessels and Piping Conference, Aug. 2020.

[10] D. Ayala-Cabrera, M. Herrera, J. Izquierdo, S.J. Ocaña-Levario, and R. Pérez-García, "GPR-Based Water Leak Models in Water Distributions Systems," Sensors, vol. 13, no. 12, Nov. 2013, pp. 15912-15936.

[11] S. Zhang, Y. Li, G. Fu, W. He, D. Hu, and X. Cai, "Wavelet Packet Analysis of Ground-Penetrating Radar Simulated Signal for Tunnel Cavity Fillings," Journal of Engineering Science and Technology Review, vol. 11, no. 6, Dec. 2018, pp. 62-69.

[12] C. Lin, X. Wang, Y. Li, F. Zhang, and Z.H. Xi, "Forward Modelling and GPR Imaging in Leakage Detection and Grouting Evaluation in Tunnel Lining," KSCE Journal of Civil Engineering, vol. 24, no. 1, Dec. 2019, pp. 278-294.

[13] R. Ahmadi, N. Fathianpour, and G.H. Norouzi, "Detecting Physical and Geometrical Parameters of Some Common Geotechnical Targets through their Effects on GPR Responses," Arabian Journal of Geosciences, vol. 8, Jul. 2014, pp. 4834-4854.

[14] A. S. Rao, M. Radanovic, Y. Liu, S. Hu, Y. Fang, K. Khoshelham, M. Palaniswami, and T. Ngo, "Real-Time Monitoring of Construction Sites: Sensors, Methods, and Applications," Automation in Construction, vol. 136, April 2022, pp. 1-22.

[15] S. Li, H. Cai, and V. Kamat, "Uncertainty-Aware Geospatial System for Mapping and Visualizing Underground Utilities," Automation in Construction, vol. 53, May. 2015, pp. 105-119.

[16] A. De Coster, J.L Pérez Medina, M. Nottebaere, K. Alkhalifeh, X. Neyt, J. Vanderdonckt, and S. Lambot, "Towards and Improvement of GPR-Based Detection of Pipes and Leaks in Water Distribution Networks," Journal of Applied Geophysics, vol. 162, Mar. 2019, pp. 139-151.

[17] N. Kim, K. Kim, Y.K. An, H.J. Lee, J.J. "Deep learning-based underground object detection for urban road pavement," International Journal of Pavement Engineering, vol. 21, no. 13, Jan. 2020, pp. 1638-1650.

[18] S. Ali, M. A. Hawwa, and U. Baroudi, "Effect of Leak Geometry on Water Characteristics Inside Pipes," Sustainability, vol. 14, no. 9, April. 2022. pp. 1-21.

[19] B. Wong, and J. A. McCann, "Failure Detection Methods for Pipeline Networks: From Acoustic Sensing to Cyber-Physical Systems," Sensors, vol. 21, no. 15, Jul. 2021. pp. 1-83.

[20] D. Ayala-Cabrera, "Characterization of Components of Water Supply Systems from GPR Images and Tools of Intelligent Data Analysis," Ph.D. thesis, Universitat Politècnica de València, Valencia (Spain), 2015.

[21] A. Akbarpour, S. Chamaani, J. Sachs, G.D. Galdo "Clutter Removal of Near-Field UWB SAR Imaging for Pipeline Penetrating Radar," IEEE J. Sel. Top. Appl. Earth Obs. Remote Sens., vol. 13, April. 2020, pp. 1527-1539.

[22] M. Rasol, J. Pais, V. Pérez-Gracia, M. Solla, F. Fernandes, S. Fontul, D. Ayala-Cabrera, F. Schmidt, H. Assadollahi, "GPR Monitoring for Road Transport Instracture, A Systematic Review and Machine Learning Insights," Construction and Building Materials, vol. 324, Mar. 2022, pp. 1-21.

[23] A. Shekargoftar, H. Taghaddos, A. Azodi, A. N. Tak, and K. Ghorab, "An Integrated Framework for Operation and Maintenance of Gas Utility Pipeline Using BIM, GIS, and AR," Journal of Performatnce of Constructed Facilities, vol. 36, no. 3, Mar. 2022.

[24] S. Li, H. Cai, and V. Kamat, "Uncertainty-Aware Geospatial System for Mapping and Visualizing Underground Utilities," Automation in Construction, vol. 53, May 2015, pp. 105-119.

[25] M. Zahlan Abdul Muthalif, D. Shojaei and K. Khoshelham, "A Review of Augmented Reality Visualization Methods for Subsurface Utilities," Advanced Engineering Informatics, vol. 51, Jan. 2022, pp. 1-18.

[26] S. Ocaña-Levario, E. Carreño-Alvarado, D. Ayala-Cabrera, J. Izquierdo, "GPR Image Analysis to Locate Water Leaks from Buried Pipes by Applying Variance Filters," Journal of Applied Geophysics, vol. 152, May. 2018, pp. 236-247.

[27] D. Ayala-Cabrera, J. Izquierdo, I. Montalvo, and R. Pérez-García, "Water supply system component evaluation from GPR radargrams using a multi-agent approach," Mathematical and Computer Modelling, vol. 57, no. 7-8, April. 2013, pp. 1927-1932.

[28] D. Ayala-Cabrera, M. Herrera, J. Izquierdo, R. Perez-Garcia, O. Piller, "A New GPR Image Analysis Proposal Based on a Multi-agent Approach and Properties of Groups – Towards Automatic Interpretations," in Proc. 8th International Congress on Environmental Modelling and Software, Toulouse, France: iEMSs, 2016, pp. 678-685.

[29] D. Ayala-Cabrera and J. Izquierdo, "GPR Image Interpretation Advancement for Smarter Technical Management of Water Leakage in Urban Water Infrastructures," in Proc. Earth Resources and Environmental Remote Sensing/GIS Applications XII, Madrid, Spain: SPIE 118630S, 2021.

[30] N. Kim, K. Kim, Y.K. An, H.J. Lee, J.J. Lee, "Deep Learning-Based Underground Object Detection for Urban Road Pavement," International Journal of Pavement Engineering, vol. 21, no. 13, 2020, pp. 1638-1650.

[31] Z. Zong, C. Chen, X. Mi, W. Sun, Y. Song, J. Li, Z. Dong, R. Huang, B. Yang, "A Deep Learning Approach for Urban Underground Objects Detection from Vehicle-Borne Ground Penetrating Radar Data in Real-Time," Int. Arch. Photogramm. Remote Sens. Spat. Inf. Sci. - ISPRS Arch., XLII-2/W16, Sep. 2019, pp. 293-299.

[32] W. Lei, J. Luo, F. Hou, L. Xu, R. Wang, and X. Jiang, "Underground Cylindrical Objects Detection and Diameter Identification in GPR B-Scans via the CNN-LSTM Framework," Electronics, vol. 9, no. 11, pp. 1804, Oct. 2020, pp. 1-16.